ELSEVIER

Polymer 43 (2002) 1657–1666

polymer

www.elsevier.com/locate/polymer

Triple layer superlattice in binary mixtures of very long *n*-alkanes: a study by SAXS

Xiangbing Zeng, Goran Ungar*

Department of Engineering Materials, University of Sheffield, Sheffield S1 3JD, UK

Received 23 August 2001; received in revised form 23 October 2001; accepted 6 November 2001

Abstract

The prevailing low-temperature phase ($T \leq 100\,^{\circ}C$) has been studied in binary mixtures of very long *n*-alkanes $C_{122}H_{246}$, $C_{162}H_{326}$, $C_{194}H_{390}$, $C_{210}H_{422}$, $C_{246}H_{494}$, $C_{258}H_{518}$ and $C_{294}H_{590}$. For alkane pairs with chain length ratio between 1.3 and 1.7 and molar ratios not too far from 1:1, the lamellar structure is that of a superlattice. Its structure is determined by small-angle X-ray scattering (SAXS), backed by calorimetry and wide-angle X-ray diffraction. One full repeat unit of the superlattice contains three crystalline layers; the two outer ones contain both long and short molecules while the middle layer contains extended interdigitated tails of the long molecules protruding from the two outer layers. This triple layer phase forms through a reversible transition on cooling from the semi-crystalline form (SCF) described by Zeng and Ungar [Macromolecules, 34 (2001) 6945]. Both forms are solid solutions in which the disparate alkane chains are intimately mixed. SCF consists of alternating crystalline and amorphous layers, the latter consisting of surplus length of the longer alkane. The transition consists of the longer molecules from two adjacent crystal layers being pulled into the intervening space and crystallizing in the form of the middle layer; at the same time the opposite ends of the chains are being aligned flush with the outer surfaces.

Keywords: Superlattice; Lamellar; Long chain

1. Introduction

Pure long chain normal alkanes [1–3] have been used for the last 15 years as ideal models for studying polymer crystallisation [4–9] and chain folding [10–14]. They are chemically the most unspecific of the model compounds used in the fundamental studies of crystalline polymers [15]. It has been established that long alkanes have a lamellar structure in the crystalline state, where the fold length of molecules is usually the integral reciprocal of the full chain length (IF form) with the chain ends and folds located at the lamellar surface [10–12]. A transient non-integer form (NIF) is found in the early stages of melt crystallisation; this transforms subsequently to IF forms [13]. NIF has a semi-crystalline lamellar structure, where only a fraction of the molecules are integer folded and fully crystallised while the other molecules traverse the crystalline layer with their tails outside as cilia in the amorphous layer [14]. The molecular arrangement in these lamellar structures are drawn in Fig. 1.

Considerably more research has been done on shorter alkanes, up to 40–50 carbon atoms, partly due to their easy availability. There has also been continuous interest and extensive work on mixtures of short *n*-alkanes since 1931 [16], concerning crystal structure [17–26], thermodynamics and phase diagrams [27–32], kinetics of crystallisation [33], chain diffusion [34–36], defects, disorder [37–41], etc. The boundary between stable and metastable solid solutions of short binary *n*-alkanes has been given by $C_{n'} = 1.20C_n - 1.60$, where $C_{n'}$ and C_n are the carbon numbers of the two components [42]. In all of the short alkane mixtures studied, the carbon number difference allowed for solid solution are not more than 10 (e.g. $C_{50}H_{102} + C_{60}H_{122}$ [19,20]), thus the inter-crystalline layers are normally confined to only several CH_2 groups at the surface.

It is only recently that sufficient quantities of long chain *n*-alkanes were synthesised [43] to allow a study of their mixtures. One of the objectives of investigating mixed long alkanes is to introduce polydispersity in a controlled way and thus bridge the gap between the information we have on monodisperse models and on polydisperse polymers. Recent experiments on crystallisation of alkane mixtures show interesting kinetic phenomena and enable us to test certain hypotheses on the mechanism of polymer

* Corresponding author. Tel.: +44-114-222-5457; fax: +44-114-222-5943.

E-mail address: g.ungar@sheffield.ac.uk (G. Ungar).

0032-3861/02/$ - see front matter
PII: S0032-3861(01)00735-2

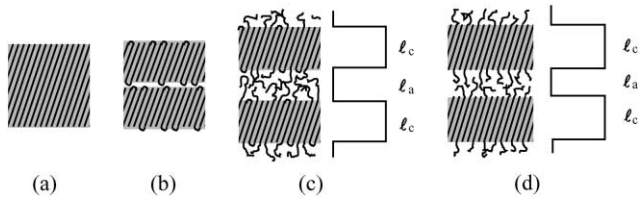

Fig. 1. Schematic representation of the molecular arrangement in different lamellar structures in melt crystallised long chain *n*-alkanes. (a) Extended chain form, (b) once-folded chain form, (c) transient non-integer folded (NIF) form, (d) semi-crystalline form (SCF). (a)–(c): pure alkane, (d) binary mixture.

crystallisation [7], 'poisoning' and 'self-poisoning' of crystal growth faces, etc. [44].

We have undertaken a structural study of various binary mixtures of pure long chain *n*-alkanes ($C_{122}H_{246}$, $C_{162}H_{326}$, $C_{194}H_{390}$, $C_{210}H_{422}$, $C_{246}H_{494}$, $C_{258}H_{518}$ and $C_{294}H_{590}$) using small-angle X-ray scattering (SAXS), differential scanning calorimetry (DSC) and Raman LAM spectroscopy. In the first paper of this series [45], it was reported that most of the binary mixtures form solid solutions in spite of the large chain length differences (up to 100 CH_2 groups) between the two components. Lamellar structure of the high temperature form of the solid solutions was found to be semi-crystalline. In this semi-crystalline form (SCF) only the short molecules are fully crystalline; they pack in crystal layers whose thickness ℓ_c is determined by the length of these molecules, appropriately corrected for chain tilt (Fig. 1d). The longer molecules mix with the shorter ones in the crystalline layers, but their surplus chain length, protruding as cilia, remains amorphous. Crystalline and amorphous layers, with thicknesses ℓ_c and ℓ_a, alternate as in the NIF structure in pure *n*-alkanes or, for that matter, as in common semi-crystalline polymers. The role of the folded chains in NIF is taken over by the shorter chains in the case of SCF in binary alkane mixtures. Unlike the case of NIF or the semi-crystalline chain-folded polymers, SCF can be the thermodynamically stable phase in the high temperature region [45].

As already noted [45], a reversible solid state transition takes place at the low temperature end of the SCF range. In the present paper, we report on the lamellar structure of the low temperature phase. The primary method used is SAXS and the proposed model is supported by the results from thermal analysis. Additional evidence from vibrational spectroscopy will be reported in the third paper of this series. Selected results of this work have appeared in a preliminary publication [46].

2. Experimental

2.1. Materials and sample preparation

The pure long chain *n*-alkanes were kindly provided by Drs G.M. Brooke and S. Mohammed, University of Durham. For details of synthesis see Ref. [43]. The alkanes used in this work are $C_{122}H_{246}$, $C_{162}H_{326}$, $C_{194}H_{390}$, $C_{210}H_{422}$, $C_{246}H_{494}$, $C_{258}H_{518}$ and $C_{294}H_{590}$. Mixtures were prepared by weighing the alkanes and mixing them in a small glass test tube and then melting them repeatedly for several minutes under nitrogen followed by quench-crystallisation. Homogeneity of mixtures was ascertained by comparing DSC and SAXS data obtained from different parts of a sample. Unless stated otherwise, the final thermal cycle of a sample prior to SAXS recording of the low-temperature phase consisted of slow cooling (0.5 °C/min) from the high-temperature phase through the transition, followed by annealing for approximately 10 h below the transition temperature (ca. 90 °C), followed finally by cooling (1 °C/min) to room temperature. The initial cooling rate for crystallisation of the high-temperature phase depended on the alkane chain length and composition; while it was kept just fast enough to prevent solidus–liquidus separation of the alkanes between the melting points of the two pure components.

2.2. Small angle X-ray scattering

The in situ SAXS experiments were performed on Station 8.2 of the Daresbury Synchrotron Radiation Source. The beam was monochromatised and double-focused onto the detector having a cross-section of $2 \times 0.3\ mm^2$ in the sample plane [47]. A high-count rate quadrant multiwire detector was used and the sample to detector distance was 3.1 m. The capillary with the sample was held in a modified Linkam hot stage with temperature control within ±0.2 °C. The beam was monitored with two ionisation chambers, one in front and one behind the sample. All diffractograms were corrected for uneven channel response by dividing them with the response to homogeneous radiation of ^{55}Fe. This also took care of the slice shape of the detector window, allowing the resulting curves to be treated as if recorded with a linear detector. The correction for positional non-linearity of the detector was done using the first 22 orders of diffraction from wet rat-tail collagen. Two third-order polynomials, linked by matching their boundary values of zeroth and first derivatives, were fitted to the inverse collagen spacings for the two halves of the detector range. A separate linearisation function was applied for each experimental session. The sample-to-detector distance in detector pixel units was calibrated using polycrystalline sample of shorter orthorhombic *n*-alkanes with precisely known unit cell lengths.

2.3. Differential scanning calorimetry

DSC experiments were performed on a Perkin–Elmer Pyris-1 instrument. Samples were sealed in 10 mm aluminium pans. Indium was used for the calibration of temperature and enthalpy. Temperature correction for isothermal and cooling cycles was derived by extrapolation of the heating rate dependence of the correction to zero or negative

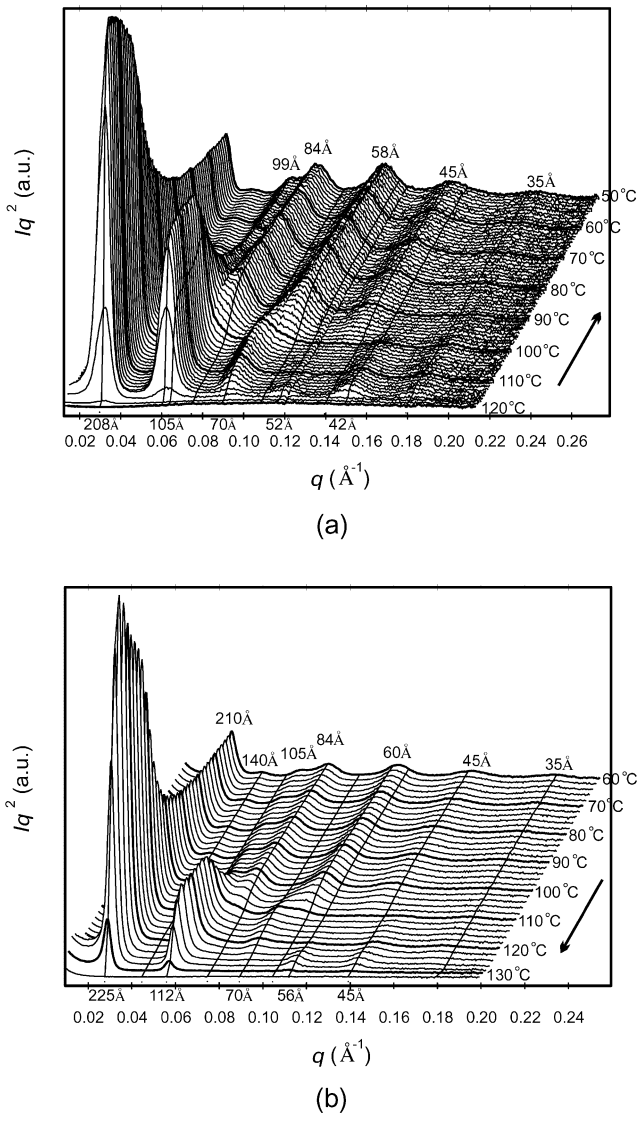

Fig. 2. Small-angle X-ray scattering curves recorded during cooling (a) and heating (b) of a binary mixture of n-$C_{162}H_{326}$ and n-$C_{246}H_{494}$ (1:1 by weight, 1.5:1 molar). The respective cooling and heating rates were 2 °C/min and 5 °C/min. Intensities are Lorentz corrected. Constant q lines ($q = 4\pi \sin(\theta/\lambda)$) are labelled by their corresponding Bragg spacings (in Å).

rates. Peak temperatures were corrected for thermal resistance [48].

3. Results

3.1. SAXS analysis

3.1.1. Experimental diffractograms

Two sequences of SAXS curves of a $C_{162}H_{326}$ + $C_{246}H_{494}$ (1:1 by weight) mixture are displayed in Fig. 2. Sequence (a) is recorded during cooling from melt and sequence (b) during heating to the melt. The two sequences are essentially reversals of each other with relatively little hysteresis (10 °C). There are two distinct temperature regions where SAXS spectra appear fundamentally different: the high temperature region between 125 and 105 °C, and the low temperature region below 100–90 °C. At high temperatures the diffraction peaks are sharp and the intensities decline steeply with increasing diffraction order. At low temperatures more peaks are present, they are also broader, and the change in intensity with diffraction order does not follow an immediately recognisable pattern. Indexing of individual diffraction peaks is also not straightforward. Annealing over many hours and sometimes days did not change the diffraction patterns of either phase to any significant extent, except for some decrease in linewidth.

The lamellar structure of the semi-crystalline high temperature phase (SCF) has been determined by SAXS previously [45,46] and described briefly in Section 1 (Fig. 1d). The SAXS pattern of the low temperature phase is quite complex. The diffraction peaks are broader and overlapping, indicating a comparatively small coherence length as expected from a phase formed through solid-state transformation. The possibility of the presence of more than one phase complicates further the indexing of diffraction peaks. The SAXS pattern also changes quite dramatically with the ratio of molecular chain lengths and composition. In the following we will concentrate on mixtures with a molar ratio of approximately 1:1, which is found to be the ideal composition for the superlattice structure as will be discussed later.

From the semi-crystalline structure model of binary solid solutions at high temperatures, it is expected that at lower temperatures the amorphous layer would tend to crystallise. It is thus possible that the solid state transformation around 105 °C is in some way associated with crystallisation of the cilia. One of the potential options is separation of molecules of different chain lengths and the formation of two types of lamellar stacks. However this is not supported by experiment, as we do not observe two series of diffraction peaks of extended forms of the two components. Another possible alternative is that the two molecular types segregate in separate lamellae, which however form stacks with a random or alternating layer sequence. The former would be analogous to the model proposed by Dorset for $C_{30}H_{62}$ + $C_{36}H_{74}$ [19,20]. However, neither option is borne out by the diffraction patterns.

Fig. 3 shows a typical small-angle diffractogram of the low temperature form, in this case of a 1:1, w/w $C_{162}H_{326}$ + $C_{246}H_{494}$ mixture. It is not immediately obvious how the strong diffraction peaks (210, 85, 60, 45 and 35 Å) should be indexed. However, in addition to these major peaks there are a number of weaker peaks and shoulders. After closer scrutiny it was recognised that a spacing of 420 Å gives a good fit for most of the peaks mentioned, even if the 420 Å peak itself is not observed. The SAXS curve has been resolved (using PeakSolve™) and as a result eight of the first 12 orders could be identified with the following Bragg spacings in Å (underlined spacings indicate clearly resolved peaks): 420, 210, 140, 105, 84, 70, 60, 52.5, 46.7,

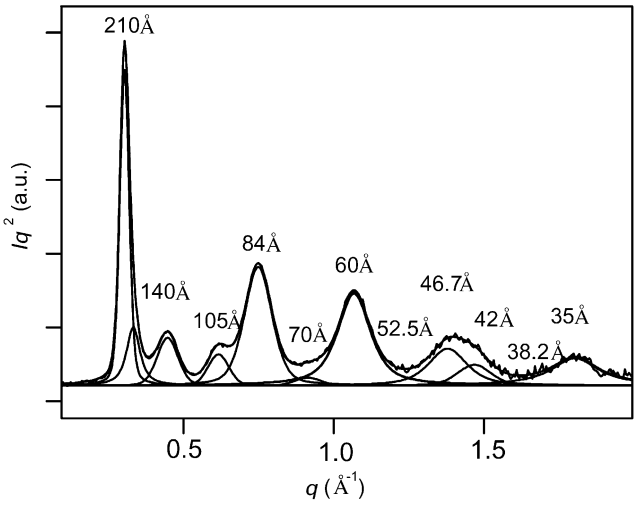

Fig. 3. Small-angle diffractogram of the 1:1, w/w mixture of $C_{162}H_{326}$ and $C_{246}H_{494}$ at room temperature. Experimental and peak-resolved traces are shown. The components are labelled by their corresponding Bragg spacings. They are all orders of the basic 420 Å periodicity.

42, 38.2 and 35. As seen in Fig. 3, a very good fit is achieved and the peak positions are well in accordance with the presumption of a structure with a 420 Å period.

While the diffraction pattern has been indexed in a satisfactory way, we now have to explain the unusually large periodicity of 420 Å, considering that the long spacings of extended chain crystals of $C_{162}H_{326}$ and $C_{246}H_{494}$ are only 170 and 258 Å. The intensity distribution among diffraction orders is similarly unusual (the absence of the first order, the strong diffraction orders 2, 5, 7, 9 and 12).

The information contained in the positions and intensities of the SAXS peaks can be used to Fourier reconstruct the one-dimensional projection of electron density and hence obtain an insight into the structure of the low-temperature form.

3.1.2. Reconstruction of electron density profiles

As the structure is that of close packed layers, with in-plane layer dimensions many times larger than the layer thickness, the diffraction pattern is determined by the one-dimensional correlation function, as in most crystalline polymers [49]. However, due to the highly periodic layer stacking the SAXS function can be treated as a series of discrete Bragg peaks. Therefore the small angle X-ray diffraction is related to the one-dimensional electron density profile normal to the lamellar stacks through Fourier series summation. Furthermore, as the structure is centrosymmetric, the profile $E(x)$ is an even periodic function and its corresponding diffraction amplitude A_n can be expressed as

$$A_0 = \frac{1}{L}\int_0^L E(x)\,\mathrm{d}x \tag{1a}$$

$$A_n = \frac{2}{L}\int_0^L E(x)\cos\left(\frac{2\pi n x}{L}\right)\mathrm{d}x, \qquad n > 0 \tag{1b}$$

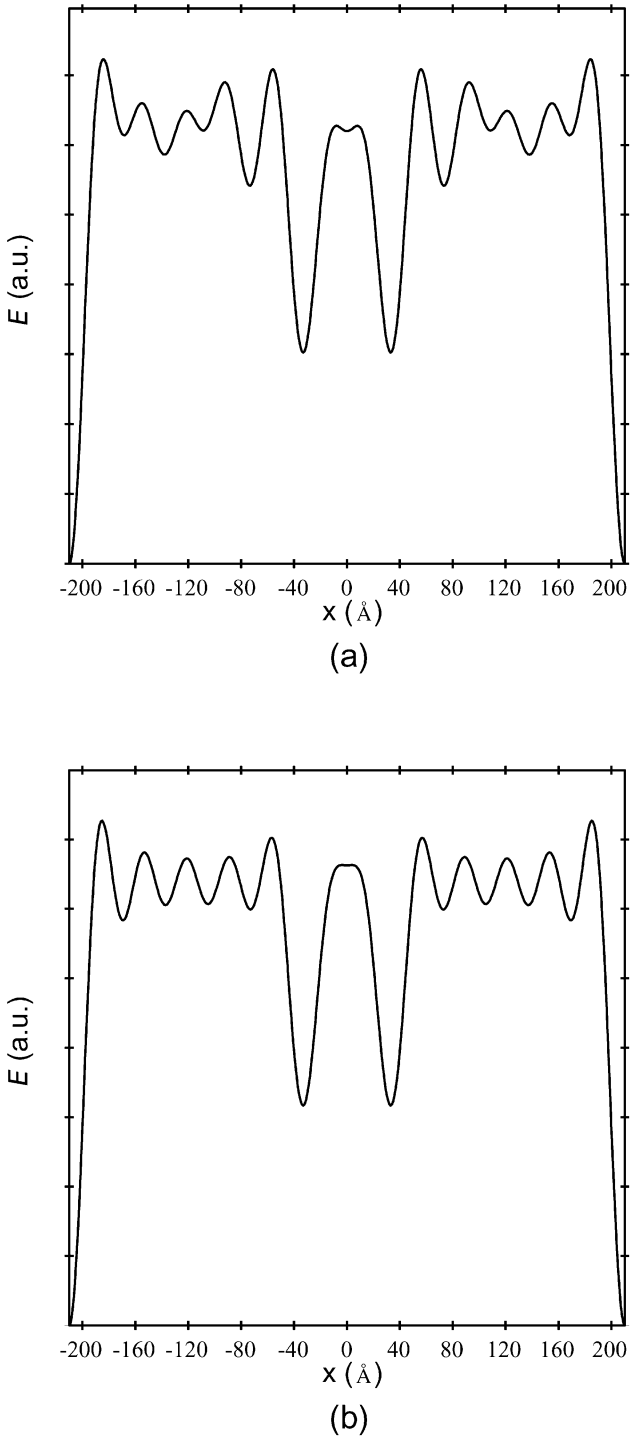

Fig. 4. Comparison of electron density profile $E_{exp}(x)$ reconstructed from experimental data (a) and $E_N(x)$ from the best-fit model (b) for $C_{162}H_{326}$ + $C_{246}H_{494}$ (1:1, w/w) mixture. $N = 12$ Fourier terms (12 orders of diffraction) were used in both reconstructions.

where L is the overall period. Conversely, $E(x)$ can be expressed in terms of A_n as:

$$E(x) = \sum_{n=0}^{\infty} A_n \cos\left(\frac{2\pi n x}{L}\right) \tag{2a}$$

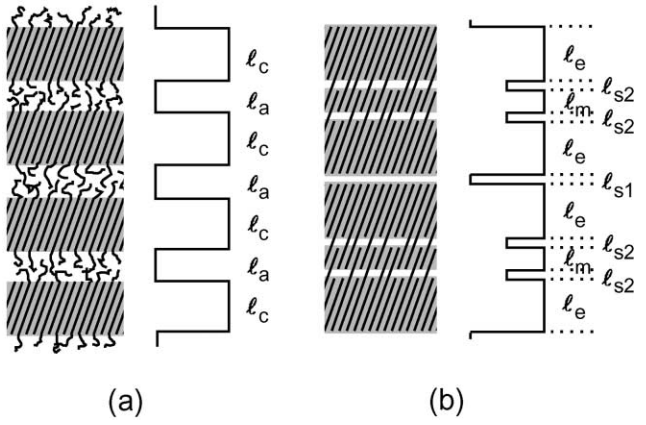

Fig. 5. Schematic representation of the molecular arrangement in (a) the high temperature semi-crystalline form (SCF) and (b) the low temperature triple-layer superlattice. In (a) the shorter chains are confined to the crystalline layer, while the surplus length of the longer chains protrudes forming the amorphous cilia layer. In (b) the shorter chains are confined to the outer two crystalline layers, while the surplus length of the longer chains coalesce in the space between, forming the third thinner crystalline layer.

or if using only the first N terms, we define

$$E_N(x) = \sum_{n=0}^{N} A_n \cos\left(\frac{2\pi n x}{L}\right) \tag{2b}$$

Experimentally we measure the intensity of the nth diffraction peak I_n (Lorentz corrected), which is equal to A_n^2, and its wavevector q_n, which is equals to $2\pi n/L$. Ideally

$$E(x) = \sum_{n=0}^{\infty} \sqrt{I_n} \cos(q_n x + \phi_n), \qquad \phi_n = 0, \pi \tag{3a}$$

Since it is impossible to measure an infinite number of diffraction orders experimentally, an approximation can be achieved with the first N orders

$$E(x) \approx E_{\exp}(x) = \sum_{n=0}^{N} \sqrt{I_n} \cos(q_n x + \phi_n), \qquad \phi_n = 0, \pi \tag{3b}$$

The phase of the structure factor, represented by ϕ, can be determined with high degree of confidence in the present case by trial and error. The electron density profile can thus be directly reconstructed from the diffraction pattern via Eq. (3b).

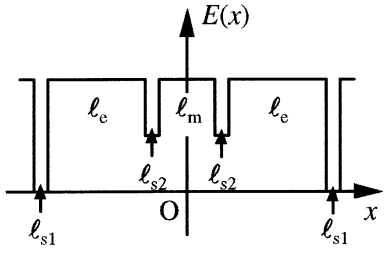

Fig. 6. Model electron density profile $E_\infty(x)$ used to fit the experimental SAXS data.

With the intensities obtained by curve resolution, different phase combinations were tried in the attempt to reconstruct a reasonable electron density profile using Eq. (3b). One of the reconstructions, with alternating amplitudes $(+ - + - + - + - + - + -)$, gives a promising electron density profile, which is shown in Fig. 4a. Neglecting the ripples caused by Fourier series truncation (see below), this $E_{\exp}(x)$ is approximately constant, except for three narrow minima: a deeper one at $x = \pm 210$ Å and two shallower ones at $x \approx \pm 30$ Å. These minima separate the high-density continuum within each period into two outer wide regions and another narrower region in the middle.

On the basis of the shape of $E_{\exp}(x)$, a working structural model of the low temperature form is assumed as follows. As illustrated in Fig. 5b, a repeat unit of the low temperature form is assumed to contain three crystalline layers. The outer two layers contain extended $C_{162}H_{326}$ chains and the best part of extended $C_{246}H_{494}$ chains mixed together. The outermost surface of each of these layers contains only chain ends, of both $C_{162}H_{326}$ and $C_{246}H_{494}$ molecules. The protruding $C_{246}H_{494}$ tails from these two layers interdigitate in the centre and form the third, thinner crystalline layer.

Taking account of such an assumed structure and of the $E_{\exp}(x)$ profile in Fig. 4a, the model electron density profile $E(x)$ is constructed as shown in Fig. 6. The three high density regions have thicknesses ℓ_e (end layers) and ℓ_m (middle layer). These three regions are separated by gaps of lower density; the outer boundary gap is set twice as deep as those bounding the middle layer, reflecting the assumption that $C_{246}H_{494}$ chains bridge these latter gaps. The widths of the deep and shallow gaps is, respectively, ℓ_{s1} and ℓ_{s2}. The thickness of all these regions and boundaries are used as adjustable parameters in the calculation of model diffraction intensities using Eqs. (1a) and (1b), which are then fitted to the experimental diffraction intensities observed. One should note that since only relative diffraction intensities were measured experimentally, the electron densities are in arbitrary units; thus the best fit to experimental data was sought with the only restriction being $\ell_{s1} + 2\ell_e + 2\ell_{s2} + \ell_m = 420$ Å.

In Fig. 7b , the best-fit model is shown for the $C_{162}H_{326}$ + $C_{246}H_{494}$ mixture (1:1 by weight). On the left, the corresponding calculated diffraction intensities are compared with the experimental ones. It is evident that the triple layer superlattice model can well explain both the unusually long period and the relative intensity distribution among diffraction orders.

Having validated the model in Fig. 6, we return to Fig. 4. Fig. 4b shows $E_N(x)$, which is the reconstruction of the best fit model $E(x)$ using the first $N = 12$ members of the cosine series (Eq. (2b)), thus matching the number of $N = 12$ diffraction orders taken into account when reconstructing the experimental density profile $E_{\exp}(x)$ (Fig. 4a). A comparison between Fig. 4a and b shows that the main cause of deviation of $E_{\exp}(x)$ from the model $E(x)$ is truncation of the series.

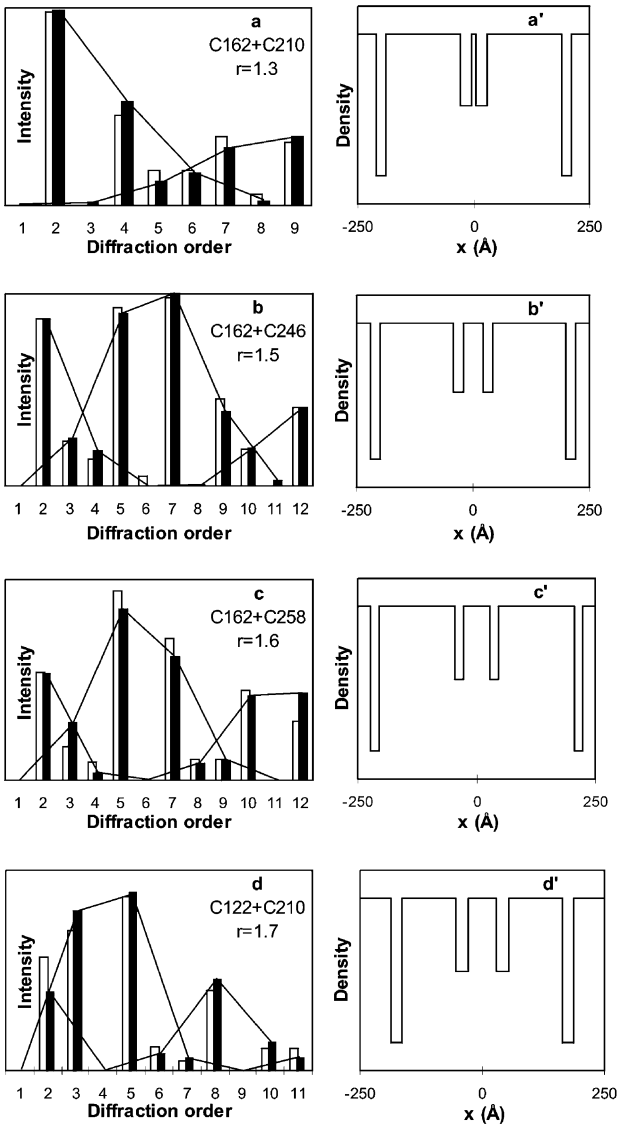

Fig. 7. Comparison of experimental (🔗) and calculated (🔗) diffraction intensities (a,b,c,d) using the corresponding model electron density profiles (a′,b′,c′,d′) consistent with the triple-layer superlattice for the low temperature phase of 1:1, w/w mixtures of (a,a′) $C_{162}H_{326} + C_{210}H_{422}$, $\ell_e = 159$ Å, $\ell_m = 10$ Å, $\ell_{s1} = 22$ Å, $\ell_{s2} = 25$ Å; (b,b′) $C_{162}H_{326} + C_{246}H_{494}$, $\ell_e = 157$ Å, $\ell_m = 45$ Å, $\ell_{s1} = 19$ Å, $\ell_{s2} = 19$ Å; (c,c′) $C_{162}H_{326} + C_{258}H_{518}$, $\ell_e = 160$ Å, $\ell_m = 57$ Å, $\ell_{s1} = 17$ Å, $\ell_{s2} = 18$ Å and (d,d′) $C_{122}H_{246} + C_{210}H_{422}$, $\ell_e = 111$ Å, $\ell_m = 56$ Å, $\ell_{s1} = 22$Å, $\ell_{s2} = 26$ Å. The intensities of the even and odd orders are joined separately by lines to show the trend of intensity change with diffraction order and also with the difference in chain length. The chain length ratio $r = l_l/l_s$ increases from 1.3 in (a) to 1.7 in (d).

The parameters of the best-fit model in Fig. 7b are listed in Table 1—see entry for $C_{162}H_{326} + C_{246}H_{494}$. The thickness of each of the end crystalline layers, $\ell_e = 157$ Å, corresponds closely to the high-density layer thickness in melt-crystallised extended chain $C_{162}H_{326}$, which is 155 Å [14,45]. This is 15 Å short of the total periodicity in pure $C_{162}H_{326}$. The thickness of the middle crystalline layer ℓ_m of 45 Å should be compared with the value of 88 Å for the surplus $C_{246}H_{494}$ chain length for 84 CH_2 groups corrected for the 35° tilt. Thus the shortfall here is 43 Å. Since the sum of the shallow dip widths $2\ell_{s2} = 38$ Å, it can be said that the inner boundary layers, containing the bridging $C_{246}H_{494}$ chains, exist at the expense of the middle crystalline layer. In other words, the degree of crystallinity of the surplus $C_{246}H_{494}$ tails is comparatively low. This conclusion is upheld by DSC and wide-angle X-ray scattering (WAXS) results described later.

In order to validate the triple layer model further, the low temperature form of three other binary mixtures were examined, two of which also contained $C_{162}H_{326}$ as the shorter component. The mixtures are $C_{162}H_{326} + C_{210}H_{422}$ (1:1.3 molar, 1:1 by weight), $C_{162}H_{326} + C_{258}H_{518}$ (1:1.6 molar, 1:1 by weight) and $C_{122}H_{246} + C_{210}H_{422}$ (1:1 molar, 1.7:1 by weight). It was found that the same electron density profile model, with different parameters, could also be used in these systems to obtain a good fit with experimental intensities. The comparison of experimental diffraction intensities with those calculated from the best-fit model are all displayed in Fig. 7 (intensity data and fitting parameters are listed in Table 1). As expected, the thickness of the crystalline end layers (ℓ_e) always corresponds to that of the shorter component of the mixture, while the thickness of the middle layer (ℓ_m) increases with the chain length difference. The chain length ratio (r) of the components in alkane mixtures in Fig. 7a–d increases, the values being 1.3, 1.5, 1.6 and 1.7. In relative terms the two shallow dips systematically move apart, resulting in the corresponding changes in the diffraction pattern. The bars representing odd and even order intensities are connected separately to bring out the trend. In the limiting case of the two shallow dips merging into one, i.e. for chain length ratio 1, the odd diffraction orders would disappear.

A similar superlattice structure is also found in the mixture $C_{194}H_{390} + C_{294}H_{590}$ (1:1, w/w, chain length ratio $r = 1.5$).

It is notable from Fig. 2 that the width of the diffraction peaks increases at the transition from the high-temperature to the low-temperature phase. Using Scherrer formula the coherence length decreases from 3.0×10^3 to 2.5×10^3 Å in the case of the $C_{162}H_{326}$–$C_{246}H_{494}$ mixture (1:1, w/w). The estimate is based on the peak width of the first strong diffraction, i.e. of the first order in the case of SCF and the second order in the case of the triple layer form. The integrated width was corrected for instrumental broadening by deconvoluting the experimental peak from that of the central beam recorded through a semi-transparent beam stop. The decrease in coherence length is consistent with a solid-state phase transformation. The significant increase in peak width with increasing diffraction order in the low-temperature phase (Fig. 3) indicates a considerable paracrystalline distortion.

Table 1
Intensity data (experimental and calculated from best-fit model) and parameters of the best-fit models for the superlattice in different alkane mixtures. The model parameters are defined in Fig. 6. R is the reliability factor defined as $(\sum_n (|A_{n,\mathrm{exp}}| - |A_{n,\mathrm{mod}}|)^2 / \sum_n |A_{n,\mathrm{exp}}|^2)^{1/2}$

Sample	Order	$C_{162}H_{326} + C_{210}H_{422}$ 1.0:1.0, w/w;1.3:1.0 molar		$C_{162}H_{326} + C_{246}H_{494}$ 1.0:1.0, w/w;1.5:1.0 molar		$C_{162}H_{326} + C_{258}H_{518}$ 1.0:1.0, w/w;1.6:1.0 molar		$C_{122}H_{246} + C_{210}H_{422}$ 1.0:1.7, w/w;1.0:1.0 molar	
		Exp.	Model	Exp.	Model	Exp.	Model	Exp.	Model
Diffraction intensities	1	0.00	0.01	0.00	0.00	0.00	0.00	0.00	0.01
	2	4.88	4.93	0.87	0.87	0.65	0.64	1.70	1.17
	3	0.00	0.06	0.23	0.25	0.20	0.34	2.10	2.40
	4	2.27	2.62	0.14	0.18	0.11	0.04	0.00	0.01
	5	0.88	0.61	0.93	0.90	1.13	1.02	2.60	2.66
	6	0.89	0.81	0.05	0.00	0.00	0.00	0.35	0.26
	7	1.75	1.44	0.98	1.00	0.85	0.74	0.15	0.18
	8	0.29	0.12	0.00	0.01	0.13	0.10	1.20	1.37
	9	1.61	1.74	0.45	0.39	0.13	0.12	0.00	0.01
	10			0.19	0.20	0.54	0.50	0.34	0.42
	11			0.00	0.03	0.00	0.00	0.34	0.18
	12			0.41	0.41	0.35	0.52		
Parameters of model (Å)	L	400		420		430		352	
	ℓ_e	159		157		160		111	
	ℓ_m	10		45		57		56	
	ℓ_{s1}	22		19		17		22	
	ℓ_{s2}	25		19		18		26	
	R	0.115		0.150		0.123		0.123	

3.2. DSC results

The relatively low crystallinity of the middle layer is supported by evidence from thermal analysis. As shown in Fig. 8, in the DSC thermogram of $C_{162}H_{326} + C_{246}H_{494}$ (1.5:1 molar; 1:1, w/w), a weak broad peak can be seen at 107 °C corresponding to the transition between the triple-layer superlattice and the SCF. The measured heat of transition is only 12 J/g, which is no more than 5% of the total enthalpy of melting; while according to our ideal model, the heat of fusion related to this transition is estimated to be around 40 J/g. The latter figure implies that the phase transition corresponds to melting of completely crystalline surplus tails of $C_{246}H_{494}$ molecules (the measured heat of fusion of fully crystallised $C_{246}H_{494}$ in the extended chain form is 260 J/g). As noted already in Section 3.1, the best-fit electron density models also suggest a low crystallinity of the middle layer since ℓ_m values are only about half the theoretical values for fully crystalline tails.

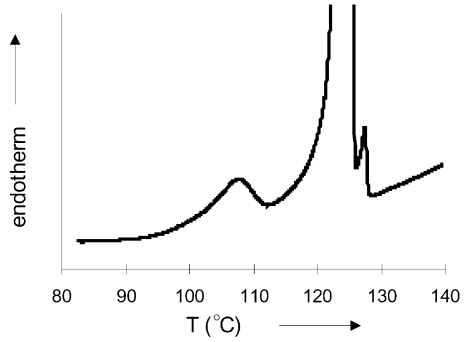

Fig. 8. DSC heating thermogram of the $C_{162}H_{326} + C_{246}H_{494}$ mixture (1:1, w/w). Heating rate 2 °C/min. Prior to the scan the sample had been cooled at 2 °C. The endotherms, in the ascending order of temperatures, correspond to the following transitions: superlattice to semi-crystalline form (107 °C), melting of the semi-crystalline form (125 °C), melting of extended chains of $C_{246}H_{494}$ formed during the heating scan (127 °C).

The low crystallinity of the middle layer is also supported by WAXS recorded simultaneously with SAXS. During the transition between SCF and the superlattice, the orthorhombic crystal structure remains unchanged. There is little change too in the intensity of the WAXS Bragg peaks, which indicates that the change in crystallinity associated with the transition is small.

3.3. Binary phase diagram

The transition temperatures between the high temperature phase and the superlattice in mixtures of $C_{162}H_{326}$ and $C_{246}H_{494}$ with different compositions are listed in Table 2. The transition temperatures were determined by both SAXS and DSC. The transition temperatures of the 1.5:1, 2.8:1 and 3.5:1 molar mixtures are fairly close, 105 ± 2 °C, which is only slightly lower than the melting point of $C_{84}H_{170}$ (110 °C) [50]. This is consistent with the transition being essentially melting of the middle layer consisting of 84 C-atom long tails.

The above transition temperature data are used here to extend to lower temperatures the binary phase diagram $C_{162}H_{326} + C_{246}H_{494}$ which had been constructed previously in the high temperature region ($T > 120$ °C) based on DSC and SAXS data [45]. The extended diagram

Table 2
Transition temperatures T_t between the high and the low temperature phase in $C_{162}H_{326}$ + $C_{246}H_{494}$ mixtures as measured by DSC and SAXS during heating. Heating rates: DSC, 2 °C/min; SAXS, 5 °C/min

Component ratio ($C_{162}H_{326}$ mol%)	33.3%	50.0%	60.0%	73.7%	77.8%
T_t (°C), DSC		119	107	103	104
T_t (°C), SAXS	120[a]	118	108	105	105

[a] Metastable.

is shown in Fig. 9. Below the temperature range shown there are no fundamental changes in phase relationships down to room temperature. Below 118 °C the superlattice is the stable phase of the system in a relatively narrow range of compositions around the ideal 1:1 molar ratio. The limits of tolerance of this phase are known only approximately. On the right (excess $C_{162}H_{326}$) the superlattice phase is limited by the close proximity of the steeply ascending SCF/(superlattice + SCF) line. On the left (excess $C_{246}H_{494}$) we can only say with certainty that mixtures with 33.3 mol% of $C_{162}H_{326}$ show additional SAXS peaks corresponding to extended-chain $C_{246}H_{494}$. It must be recognised that it is difficult to discern small amounts of an additional phase in the SAXS spectra due to the broadness of diffraction peaks at lower temperatures. Another conspicuous feature of the phase diagram is the steep increase in the SCF-superlattice transition temperature as the concentration of $C_{162}H_{326}$ decreases from 60 to 50 mol%.

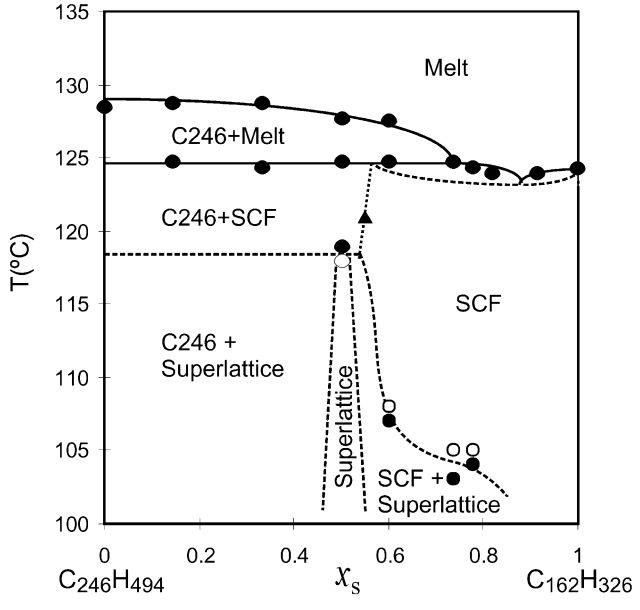

Fig. 9. Binary phase diagram of the $C_{162}H_{326}$ + $C_{246}H_{494}$ system. Full circles: data from DSC; empty circles: data from SAXS; full triangle: from DSC using lever rule as described in Ref. [45]. The part of the diagram above 120 °C has already been described in Ref. [45]. Dashed lines are determined with less certainty than full lines.

4. Discussion

In this paper we have focused on binary mixtures with a chain length ratio from 1.3 to 1.7 and a component molar ratio around 1:1. Under these conditions the triple layer superlattice is found to be the low-temperature phase. Under other circumstances in some binary systems there are still other low-temperature forms, the structure of which has not yet been solved. When the chain length difference is smaller, e.g. in the $C_{162}H_{326}$ + $C_{194}H_{390}$ mixture (1:1 molar ratio, chain length ratio 1.2), a distinct solid state transition from the SCF has been found at a lower temperature. However, the SAXS diffraction pattern of the low temperature phase cannot be explained by the triple layer model used above. The problem is further complicated by the presence of different chain tilt angles in such mixtures, e.g. it is observed in mixtures of $C_{162}H_{326}$ and $C_{246}H_{494}$ (3:1 and 7:1 by weight) that a perpendicular extended-chain form appears on slow cooling at lower temperatures.

According to the superlattice model in Fig. 5b, the short and long molecules of the two components are paired but otherwise randomly positioned within the common layer structure; they are not phase separated. A high degree of crystallinity is thus maintained, close to that of the phase separated extended chain crystal, while a high proportion of the entropy of mixing is preserved at the same time.

It is interesting to consider the transformation mechanism of the high temperature SCF to the triple layer superlattice. We envisage that initially some local crystallisation takes place in an amorphous layer of the SCF. This pulls in molecules of the longer alkane until the chain ends at the opposite side are flush with the outer surface of the two existing crystalline layers. The driving force for this is crystallisation of the middle layer. Once the first triple layer unit is thus created, the transition spreads in a co-operative fashion. The high degree of regularity in layer stacking is ensured by the fact that once a significant number of cilia had been removed from the outer amorphous layers, these become non-viable for crystallisation as they lack the necessary material for space filling. The transformation to the superlattice thus propagates by crystallisation of alternative amorphous layers. On heating, the transition to SCF can be regarded as melting of the thinner middle layers. This frees up the molecules of the longer alkane to move longitudinally, acquiring additional entropy $R \ln(n_l - n_s)$ (n_l and n_s are the carbon numbers in the long and the short alkane; see Ref. [45], Eq. (8b)). Hence an amorphous layer between each crystalline layer in SCF.

An alternative potential structural model for mixtures of $C_{162}H_{326}$ and $C_{246}H_{494}$ was considered initially, as shown in Fig. 10. We note that the chain length ratio of these two alkanes is 2:3. According to this alternative model molecules of $C_{246}H_{494}$ are folded asymmetrically into one third (82 carbons) and two thirds of their length (164 carbons), rather than into two halves as in the once-folded form

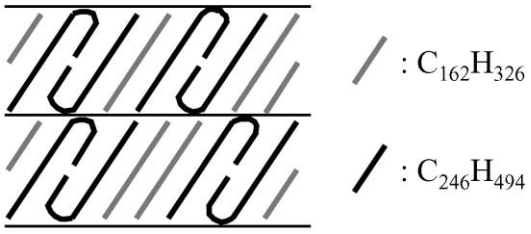

Fig. 10. Alternative model of co-crystallised $C_{162}H_{326}$ + $C_{246}H_{494}$ mixture with $C_{246}H_{494}$ molecules asymmetrically folded. This model is not supported by experiment.

(Fig. 1b). A pair of such $C_{246}H_{494}$ molecules, with one fold up and the other facing down, could be easily incorporated into a $C_{162}H_{326}$ lamella with smooth surfaces. Although such a structure is shown to be incorrect in the case of the low temperature form in the mixtures described in this paper, asymmetric folding may not be completely ruled out elsewhere. However, by failing to materialise in these, almost ideal circumstances, the mode of chain-folded crystallisation where one molecule follows another within the crystal lamella [13,51,52] has its credibility diminished. In fact in all long alkane structures observed so far chain ends have been segregated out to the crystal surface or to the amorphous phase [15]. If at all viable, such a crystallisation mode may have the best chance in polymers with interacting ends, such as hydroxy-terminated poly(ethylene oxide) [53].

Moving to the binary phase diagram in Fig. 9, the role of the superlattice can be formally compared to that of an intermetallic compound in a metallurgical phase diagram, or of a stable chemical complex in a chemical composition diagram. Regarding the steep increase in the SCF-superlattice transition temperature between 60 and 50 mol% $C_{162}H_{326}$, our proposed explanation is the same as that suggested previously [45] for the position of the phase boundary SCF/(SCF + extended $C_{246}H_{494}$). It is due to the steep increase in free energy of SCF arising from steric overcrowding at the crystal–amorphous interface as the number of $C_{246}H_{494}$ chains entering the amorphous phase, with their expanded effective cross-section, reaches the critical value (the 'gambler's ruin' problem [54]).

In some of the solid solutions of short *n*-alkanes, i.e. $C_{30}H_{62}$ + $C_{36}H_{74}$, [22] $C_{30}H_{62}$ + $C_{40}H_{82}$ [23] and $C_{28}H_{58}$ + $C_{36}H_{74}$ [27] superlattices or modulated structures were found at ambient temperature. In most cases molecules of different chain length are considered to crystallise separately in different layers (micro-phase separation) and these layers are then packed randomly or non-randomly [19,20]. Similarities can be drawn between some of the models proposed [22,23] with our superlattice model, but the crucial difference is that the two components in short alkane tend to segregate rather than mix within the same crystalline layer. Further studies are required in order to complete the picture of alkane mixtures from short to long chains.

The triple layer form described here is to some extent related to the 'folded-extended' or 'mixed integer' form recently found in pure *n*-alkane $C_{210}H_{422}$ [55] and in $C_{122}H_{246}$ + $C_{246}H_{494}$ mixtures (Fig. 11) [56]. $C_{210}H_{422}$, which had crystallised in the NIF state (Fig. 1c), transforms isothermally or on cooling to the folded–extended (FE) form rather than to the once-folded form as in the case of $C_{246}H_{494}$ and longer alkanes (Fig. 1b). The FE form is another triple layer phase but with all three layers having the same thickness. The role of the short alkane in the present mixtures is taken up in the FE form by folded chains. Thus the ratio of the effective chain lengths is 1:2. According to our model of the FE form, the folded chains are located in the two outer layers. The overall repeat of this superlattice is given by the sum of the lengths of an extended and a folded chain, i.e. 1.5 chain lengths. A similar structure exists in $C_{122}H_{246}$ + $C_{246}H_{494}$ mixtures where $C_{122}H_{246}$ chains, which are half as long as those of $C_{246}H_{494}$, serve to fill any vacancy arising from irregular packing of extended and folded chains of $C_{246}H_{494}$.

The existence of the FE form, where *n*-alkane molecules with different fold conformation and different chain lengths can co-crystallise, indicates that the upper limit of the chain length ratio of miscible *n*-alkanes could go well above the value of 1.7 observed in this work, where both components are in the extended chain conformation. It is suggested that *n*-alkanes with very different chain lengths can co-crystallise, with the longer chains being folded once, twice or more times. Experiments are underway to test this.

Finally, the triple layer structure, the high-temperature SCF and the transition between them have a parallel in secondary crystallisation and premelting of polydisperse polymers. The formation of 'dominant' lamellae and subsequent formation of in-filling lamellae in the remaining uncrystallised regions during spherulite formation have been well documented [57]. Similarly, thin lamellae formed during secondary crystallisation may melt at a temperature significantly lower than the melting point of the bulk of the material, causing broadening of the melting endotherm, a

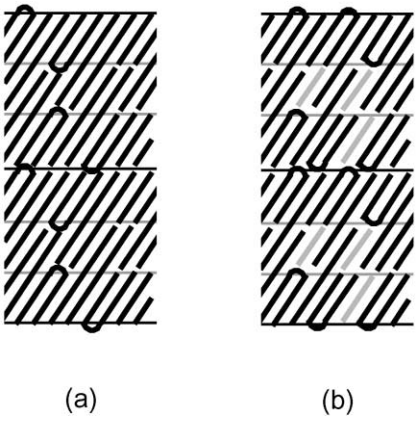

Fig. 11. Schematic drawing of the FE forms observed in pure $C_{210}H_{422}$ and $C_{198}H_{398}$ [55] (a) and in $C_{122}H_{246}$ + $C_{246}H_{494}$ binary mixtures [56] (b). Two triple-layer units are shown in each case. The pale lines in (b) indicate molecules of $C_{122}H_{246}$.

low 'softening point' and sometimes additional low-temperature endotherms [58,59].

5. Conclusions

A triple layer superlattice is found to be the structure of the low temperature phase of several binary solid solutions of very long chain *n*-alkanes with a chain length ratio between 1.3 and 1.7 and a chain length difference up to 100 ℃ atoms. One full repeat unit of the superlattice contains three crystalline layers; the two outer ones contain both long and short molecules while the middle layer contains extended interdigitated tails of the long molecules protruding from the two outer layers. In this phase, observed generally below about 100 ℃, crystallinity is high while molecules of the two species are still mixed, thus energy is low and entropy is high. The solid state transition from the high temperature SCF to this low temperature superlattice provides a good model for secondary crystallisation of polymers, and the reverse of it a model for pre-melting.

Acknowledgements

We are greatly indebted to Dr G.M. Brooke of University of Durham for the samples of long chain *n*-alkanes. We also thank Mr A. Gleeson of Daresbury Laboratory for the help with setting up the SAXS experiments. We thank the EPSRC and the Petroleum Research Fund, administered through American Chemical Society, for financial support.

References

[1] Bidd I, Whiting MC. J Chem Soc Chem Commun 1985:543.
[2] Bidd I, Holdup DW, Whiting MC. J Chem Soc Perkin Trans 1 1987:2455.
[3] Lee KS, Wegner G. Makromol Chem, Rapid Commun 1985;6:203.
[4] Ungar G, Keller A. Polymer 1987;28:1899.
[5] Organ SJ, Keller A, Hikosaka M, Ungar G. Polymer 1996;37:2517.
[6] Organ SJ, Barham PJ, Hill MJ, Keller A, Morgan RL. J Polym Sci, Pt B: Polym Phys 1997;35:775.
[7] Hosier IL, Bassett DC, Vaughan AS. Macromolecules 2000;33:8781.
[8] Ungar G, Mandal P, Higgs PG, de Silva DSM, Boda E, Chen CM. Phys Rev Lett 2000;85:4397.
[9] Ungar G, Putra EGR. Macromolecules 2001;34:5180.
[10] Ungar G, Stejny J, Keller A, Bidd I, Whiting MC. Science 1985;229:386.
[11] Organ SJ, Keller AJ. Polym Sci Polym Phys Ed 1987;25:2409.
[12] Ungar G, Organ SJ, Keller A. J Polym Sci Polym Phys Ed 1988;26:259.
[13] Ungar G, Keller A. Polymer 1986;27:1835.
[14] Zeng XB, Ungar G. Polymer 1998;39:4523.
[15] Ungar G, Zeng XB. Chem Rev 2002 in press.
[16] Piper SH, Chibnall AC, Hopkins SJ, Pollard A, Smith JAB, Williams EF. Biochem J 1931;25:2072.
[17] Smith AE. Acta Crystallogr 1957;10:802.
[18] Luth H, Nyburg SC, Robingson PM, Scott HG. Mol Cryst Liq Cryst 1974;27:337.
[19] Dorset DL. Macromolecules 1985;18:2158.
[20] Dorset DL. Macromolecules 1986;19:2965.
[21] Gerson AR, Nyburg SC. Acta Crystallogr B 1994;50:252.
[22] Dorset DL, Snyder RG. J Phys Chem 1996;100:9848.
[23] Dorset DL. J Phys Chem B 1997;101:4870.
[24] Chevallier V, Provost E, Bourdet JB, Bouroukba M, Petitjean D, Dirand M. Polymer 1999;40:2121.
[25] Gerson AR, Nybrug SC, McAleer A. J Appl Cryst 1999;32:296.
[26] Gilbert EP. Phys Chem Chem Phys 1999;1:1517, see also pages 2715, 5209.
[27] Bonsor DH, Bloor D. J Mater Sci 1977;12:1559.
[28] Asbach GI, Geiger K, Wilke W. Colloid Polym Sci 1982;260:151.
[29] Denicolo I, Craievich AF, Doucet J. J Chem Phys 1984;80:6200–3.
[30] Dorset DL. Macromolecules 1987;20:2782.
[31] Dorset DL. Macromolecules 1990;23:623.
[32] Rajabalee F, Metivaud V, Mondieig D, Haget Y, Cuevas-Diarte MA. J Mater Res 1999;14:2644.
[33] Lauritzen JI, Passaglia E, Dimarzio E. J Res Nat Bur Stand A 1967;71:245.
[34] Ungar G, Keller A. Colloid Polym Sci 1979;257:90.
[35] Zerbi G, Piazza R, Holland-Moritz K. Polymer 1982;23:1921.
[36] Yamamoto T, Aoki H, Miyaji S, Nozaki K. Polymer 1997;38:2643.
[37] Craievich A, Doucet J, Denicolo I. J Phys 1984;45:1473.
[38] Maroncelli M, Strauss HL, Snyder RG. J Phys Chem 1985;89:5260.
[39] Kim Y, Strauss HL, Snyder RG. J Phys Chem 1989;93:485.
[40] Basson I, Reynhardt EC. J Chem Phys 1991;95:1215.
[41] Clavell-Grunbaum D, Strauss HL, Snyder RG. J Phys Chem B 1997;101:335.
[42] Dorset DL, Snyder RG. Macromolecules 1995;28:8412.
[43] Brooke GM, Burnett S, Mohammed S, Proctor D, Whiting MC. J Chem Soc, Perkin Trans 1 1996:1635.
[44] de Silva DSM, Ungar G. Presented at European Polymer Conference Crystallization of Polymers, Gargnano, Italy, June 2000; submitted for publication.
[45] Zeng XB, Ungar G. Macromolecules 2001;34:6945.
[46] Zeng XB, Ungar G. Phys Rev Lett 2001;86:4875.
[47] Zerbi G, Magni R, Gussoni M, Holland-Moritz K, Bigotto A, Dirlikov S. J Chem Phys 1981;75:3175.
[48] Hohne GWH, Hemminger W, Flammersheim H-J. Differential scanning calorimetry, an introduction for practitioners. Berlin: Springer, 1996.
[49] Vonk CG, Kortleve G. Kolloid Z Z Polym 1967;220:19.
[50] Takamizawa K, Ogawa Y, Oyama TO. Polym J 1982;14:441.
[51] Kern W, Davidovits J, Rautekus KJ, Schmidt GF. Makromol Chem 1961;43:106.
[52] Keller A. Lecture Presented at Symposium 'La Vie', Société de la Vie, Palais de Versailles, June 1977.
[53] Cheng SZD, Chen JH, Zhang AQ, Barley JS, Habenschuss A, Schack PR. Polymer 1992;33:1140.
[54] DiMarzio EA, Guttman CM. Polymer 1980;21:733.
[55] Zeng XB, Ungar G, Spells SJ. Polymer 2000;41:8775.
[56] Zeng XB, Ungar G. unpublished.
[57] Bassett DC. Phil Trans R Soc A (Lond) 1994;348:29.
[58] Blundell DJ. Polymer 1987;28:2248.
[59] Bassett DC, Olley RH, Al Raheil IAM. Polymer 1988;29:1745.